

SDSS J1058+5443: A blue quasar does not have optical/NUV broad emission lines

XUEGUANG ZHANG^{*1} AND SIDAN ZHAO²

¹*School of Physical Science and Technology, GuangXi University, No. 100, Daxue Road, Nanning, 530004, P. R. China*

²*School of Physics and technology, Nanjing Normal University, No. 1, Wenyuan Road, Nanjing, 210023, P. R. China*

(Accepted September 7, 2022)

Submitted to ApJ

ABSTRACT

In the manuscript, the blue quasar SDSS J105816.19+544310.2 (=SDSS J1058+5443) at redshift 0.479 is reported as so-far the best candidate of true type-2 quasar with disappearance of central BLRs. There are so-far no definite conclusions on the very existence of true type-2 AGN, mainly due to detected optical broad emission lines in high quality spectra of some previously classified candidates of true type-2 AGN. Here, not similar as previous reported candidates for true type-2 AGN among narrow emission-line galaxies with weak AGN activities but strong stellar lights, the definite blue quasar SDSS J1058+5443 can be well confirmed as a true type-2 quasar due to apparent quasar-shape blue continuum emissions but apparent loss of both the optical broad Balmer emission lines and the NUV broad Mg II emission line. Based on different model functions and F-test statistical technique, after considering blue-shifted optical and UV Fe II emissions, there are no apparent broad optical Balmer emission lines and/or broad NUV Mg II line, and the confidence level is smaller than 1sigma to support broad optical and NUV emission lines. Moreover, assumed the Virialization assumption to broad line emission clouds, the re-constructed broad emission lines strongly indicate that the probable intrinsic broad emission lines, if there were, cannot be hidden or overwhelmed in the noises of SDSS spectrum of SDSS J1058+5443. Therefore, SDSS J1058+5443, so-far the best and robust candidate of true type-2 quasar, leads to the further clear conclusion on the very existence of true type-2 AGN.

Keywords: galaxies:active – galaxies:nuclei – quasars:emission lines – quasars:individual(SDSS J1058)

1. INTRODUCTION

Type-1 AGN (broad line Active Galactic Nuclei) and type-2 AGN (narrow line AGN) are the two main classes of AGN, due to quite different spectroscopic emission line features. The constantly being improved Unified Model (Antonucci 1993; Netzer 2015) has been widely accepted to explain the different observational phenomena between type-1 and type-2 AGN: central AGN continuum emissions and broad line emissions from central broad emission line regions (BLRs) are seriously obscured by central dust torus in type-2 AGN. And the well detected polarized broad emission lines in type-2 AGN, such as the results well discussed in Antonucci & Miller (1985); Tran (2001, 2003); Savic et al. (2018), provide robust evidence to strongly support the Unified Model, indicating that type-1 and type-2 AGN have the same central geometric structures including similar BLRs, but central BLRs hidden in type-2 AGN.

Interestingly, based on the pioneer work on studying polarized broad emission lines in type-2 AGN in Antonucci & Miller (1985); Tran (2001, 2003); Nagao et al.

(2004); Cardamone et al. (2007) and then followed in Shi et al. (2010); Barth et al. (2014); Zhang (2014); Li et al. (2015); Pons & Watson (2016); Zhang et al. (2021c), there is one special kind of AGN: true type-2 AGN (or AGN with none hidden-BLRs, or BLRs-less AGN or unobscured type-2 AGN in the literature), which have no expected hidden central BLRs. There are about 30 Seyfert 2 galaxies with no hidden BLRs reported in Tran (2001, 2003), due to lack of polarized broad emission lines. There are two strong candidates of true Type-2 AGN, NGC3147 and NGC4594, reported in Shi et al. (2010), due to their few X-ray extinctions and the upper limits on the broad emission line luminosities are two orders of magnitude lower than the average of typical Type-1 AGN. A small number of Type-2 quasar are reported in Barth et al. (2014) through their strong g-band variabilities. A sample of candidates of true Type-2 AGN are reported in Zhang (2014), through both their the long-term variability and the expected reliable power law components in their spectra in SDSS (Sloan Digital Sky Survey). A candidate of true Type-2 AGN, SDSS J0120, is reported in Li et al. (2015),

through its long-term variability properties but none-detected broad emission lines. A small sample of candidates of true Type-2 AGN are reported in Pons & Watson (2016) based on their properties of unobscured X-ray emissions. More recently, Zhang et al. (2021c) reported the composite galaxy SDSS J1039 as a candidate of true type-2 AGN, based on its long-term variabilities and its apparent loss of broad optical Balmer emission lines.

Meanwhile, there are different physical models proposed to explain the disappearance of central BLRs, such as the well reported models in Nicastro et al. (2003); Elitzur & Ho (2009); Cao (2010); Ichikawa et al. (2015); Elitzur & Netzer (2016), strongly indicating disappearance of central normal BLRs depending on physical properties of central AGN activities and/or depending on properties of central dust obscuration. Nicastro et al. (2003) have shown that absence or presence of central BLRs can be well regulated by accretion rate, assumed the BLRs formed by accretion disk instabilities. Elitzur & Ho (2009) have proposed a disk-wind scenario to predict the disappearance of the central BLRs at quite low luminosities. Cao (2010) has shown that disappearance of central BLRs associated with the outflows from the accretion disks can be expected in AGN with Eddington ratio smaller than 0.001. Elitzur & Netzer (2016) have shown that disappearance of central BLRs could be expected in AGN with higher luminosities than $4 \times 10^{46} \text{erg s}^{-1}$ considering mass conservations in the disk outflows.

However, detailed study on reported candidates of true type-2 AGN questions the very existence of true type-2 AGN, such as the detailed study in Mrk573 and NGC3147. Tran (2001) has classified Mrk573 as a candidate of true type-2 AGN, however Nagao et al. (2004) have shown the clearly detected polarized broad Balmer lines, leading Mrk573 as a normal type-2 AGN with central hidden BLRs. Similarly, Shi et al. (2010); Bianchi et al. (2012) have classified NGC3147 as a candidate of true type-2 AGN through both spectropolarimetric results and unobscured X-ray emission properties, however Bianchi et al. (2019) more recently have clearly detected double-peaked broad $H\alpha$ in high quality HST spectrum. Furthermore, Ichikawa et al. (2015) have well discussed that none detected polarized broad emission lines in candidates of some true type-2 AGN may probably due to effects of less scattering medium and/or due to effects of the increased torus obscurations.

Besides true type-2 AGN with loss of central BLRs as a precious subclass of AGN, there is one another precious subclass of AGN: weak-line quasars which have quite weak broad emission lines in UV-optical band. Since the first sample of 74 high redshift ($z > 3$) weak-line quasars in SDSS reported in Diamond-Stanic et al. (2009), weak-line quasars are interesting targets to provide further clues on accretion disk formation and/or abnormal properties of central BLRs

for high ionization emission lines, such as in Shemmer et al. (2010); Plotkin et al. (2015); Marlar et al. (2018); Paul et al. (2022). However, among the reported weak-line quasars identified by UV emission line properties, optical Balmer emission line ($H\alpha$ and $H\beta$) properties have been checked and reported in dozens of weak-line quasars, such as the results in Plotkin et al. (2015) and the reported virial BH masses of weak-line quasars by properties of broad Balmer lines in Marculewicz & Nikolajuk (2020), indicating there are apparent broad Balmer emission lines (large rest-frame equivalent widths) in weak-line quasars. Therefore, weak-line quasars with quite weak UV emission lines (especially $\text{Ly}\alpha$ and C IV) but apparent broad Balmer lines are not similar as true type-2 AGN with none-detected broad Balmer lines, and there are no further descriptions and discussions on weak-line quasars in the manuscript.

There is so-far no definite conclusion on the very existence of true type-2 AGN because of lower quality spectra with larger noises being applied to explain the undetected broad emission lines, but **to detect true type-2 AGN in high luminous blue AGN** would provide more clearer clues on the very existence of true type-2 AGN. Here, we report one candidate of true type-2 AGN in the blue quasar SDSS J1058+5443 with none detected broad emission lines, which will provide robust evidence to support the very existence of true type-2 AGN. And due to none-detected broad Balmer lines, there are no further discussions on the SDSS J1058+5443 as one weak-line quasar in the manuscript. Section 2 presents our main results on spectroscopic properties of SDSS J1058+5443, to provide strong evidence to support disappearance of broad optical and NUV emission lines. Section 3 gives properties of BH mass of SDSS J1058+5443. Section 4 shows the necessary discussions. Section 5 gives our final summaries and conclusions. And we have adopted the cosmological parameters $H_0 = 70 \text{km} \cdot \text{s}^{-1} \text{Mpc}^{-1}$, $\Omega_\Lambda = 0.7$ and $\Omega_m = 0.3$.

2. SPECTROSCOPIC PROPERTIES OF SDSS J1058+5443

SDSS J1058+5443 at redshift 0.479 is a well classified blue quasar in SDSS, with its spectrum shown in Fig. 1. The blue continuum emissions from NUV to NIR can be well described by a power law $f_\lambda \propto (\lambda)^{-1.65 \pm 0.01}$ with the continuum luminosity at rest wavelength 5100\AA to be (about $\lambda L_{5100} \sim (5.74 \pm 0.06) \times 10^{44} \text{erg/s}$, leading SDSS J1058+5443 to be a definitely blue quasar. Meanwhile, the narrow emission lines, especially the apparent $[\text{O III}]\lambda 4959, 5007\text{\AA}$ doublet, can be well applied to totally confirm the redshift $z \sim 0.479$. Moreover, the composite spectrum of SDSS quasars reported in Vanden Berk et al. (2001) is also shown in Fig. 1, providing interesting clues on the apparent blue continuum emission features of SDSS J1058+5443. More interestingly, besides the quasar-shape power law continuum emissions, it looks

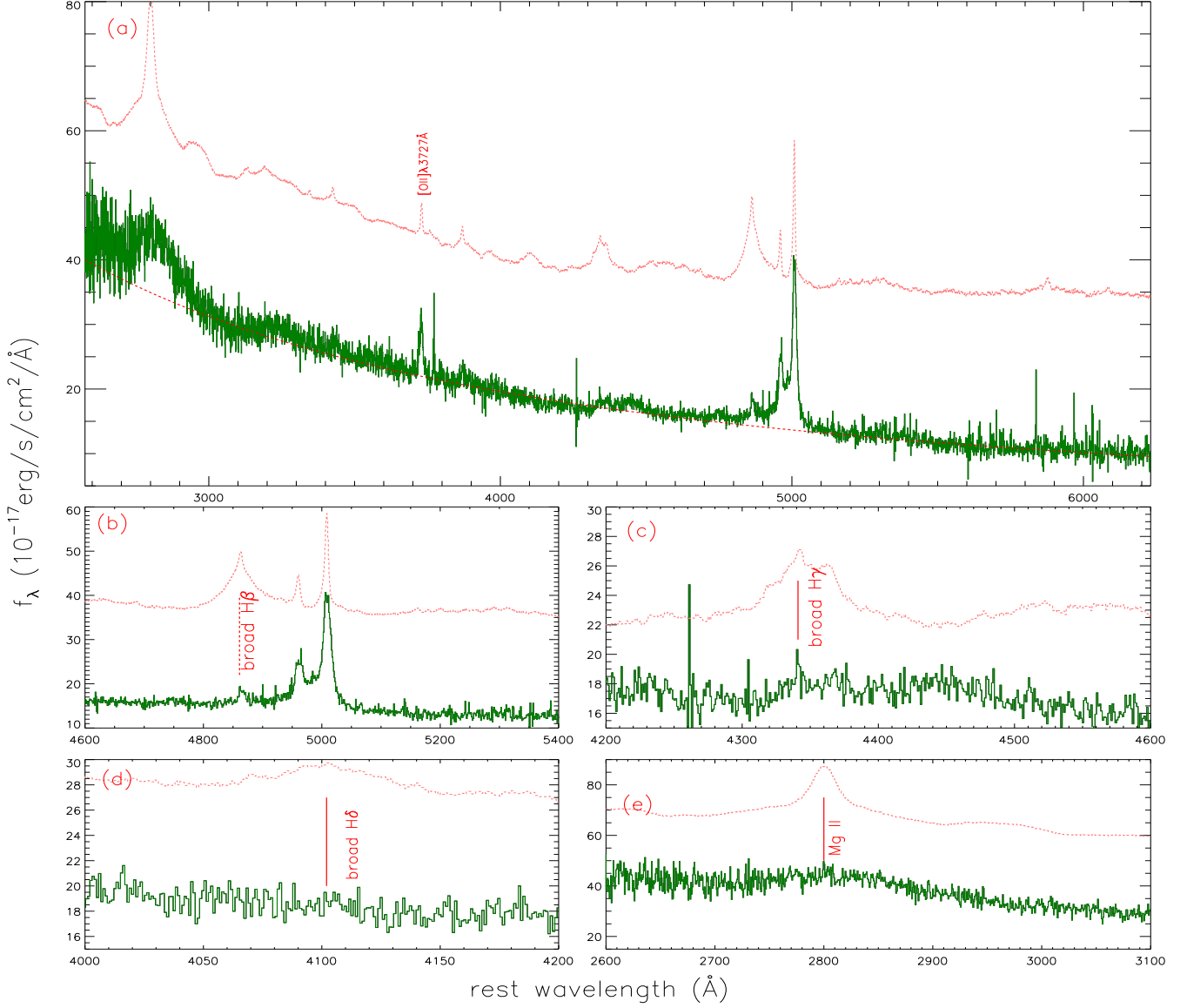


Figure 1. Panel (a) shows the whole SDSS spectrum of SDSS J1058+5443 (solid dark green line) and the composite spectrum of SDSS quasars (dashed pink line). Dashed red line shows the power law component to describe the continuum emissions. Panel (b), (c), (d) and (e) show the spectrum (solid dark green line) around H β (rest wavelength from 4600 to 5400Å), H γ (rest wavelength from 4250 to 4500Å), H δ (rest wavelength from 4000 to 4200Å) and Mg II (rest wavelength from 2600 to 3100Å) and the composite spectrum of SDSS quasars (dashed pink line), respectively. Vertical red lines mark the positions of the expected broad H β , broad H γ , broad H δ and broad Mg II lines in the Panel (b), (c), (d) and (e).

like that there are no broad optical Balmer emission lines and no broad NUV Mg II line but apparent Fe II emissions in the SDSS J1058+5443, especially based on the shown detailed emission features around H β , around H γ , around H δ and around Mg II line in the panel (b), (c), (d), and (e) in the Fig. 1.

2.1. Properties of optical Balmer lines

Besides the direct comparisons between the SDSS spectroscopic emission line features and the emission line features

in the composite spectrum of SDSS quasars, shown in Fig. 1, the detailed properties of the line emissions around the expected broad emissions lines are well measured by Gaussian functions as follows. Before proceeding further, there is one point we should note. There is a very broad emission component around 4450Å, however, so broad component is not existed around H β , indicating the broad component should be not from Balmer emission clouds. Therefore, in order to well check properties of the very broad component around 4450Å, the emission properties with rest wavelength range from 4200

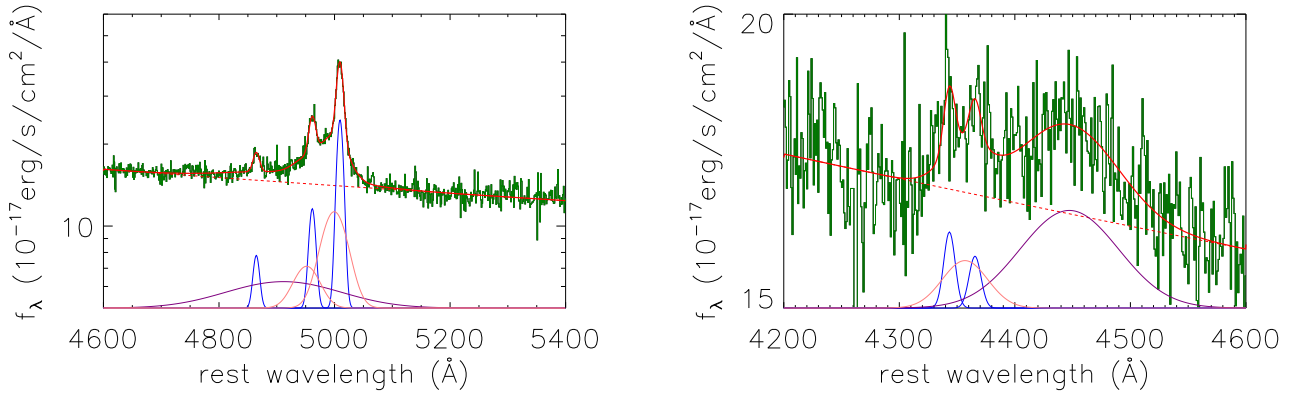


Figure 2. Best-fitting results to the emission lines around $H\beta$ (left panel) and around $H\gamma$ (right panel) by model A. In each panel, solid dark green line shows the SDSS spectrum, solid red line shows the best-fitting results, dashed red line shows the determined power law continuum emissions, solid blue lines show the determined narrow Balmer line and core components of $[O\ III]$ emissions, solid pink lines show the determined extended components of $[O\ III]$ emissions, solid purple line shows the determined broad emission component. In order to show clearer results, the Y-axis is in logarithmic coordinate in each panel.

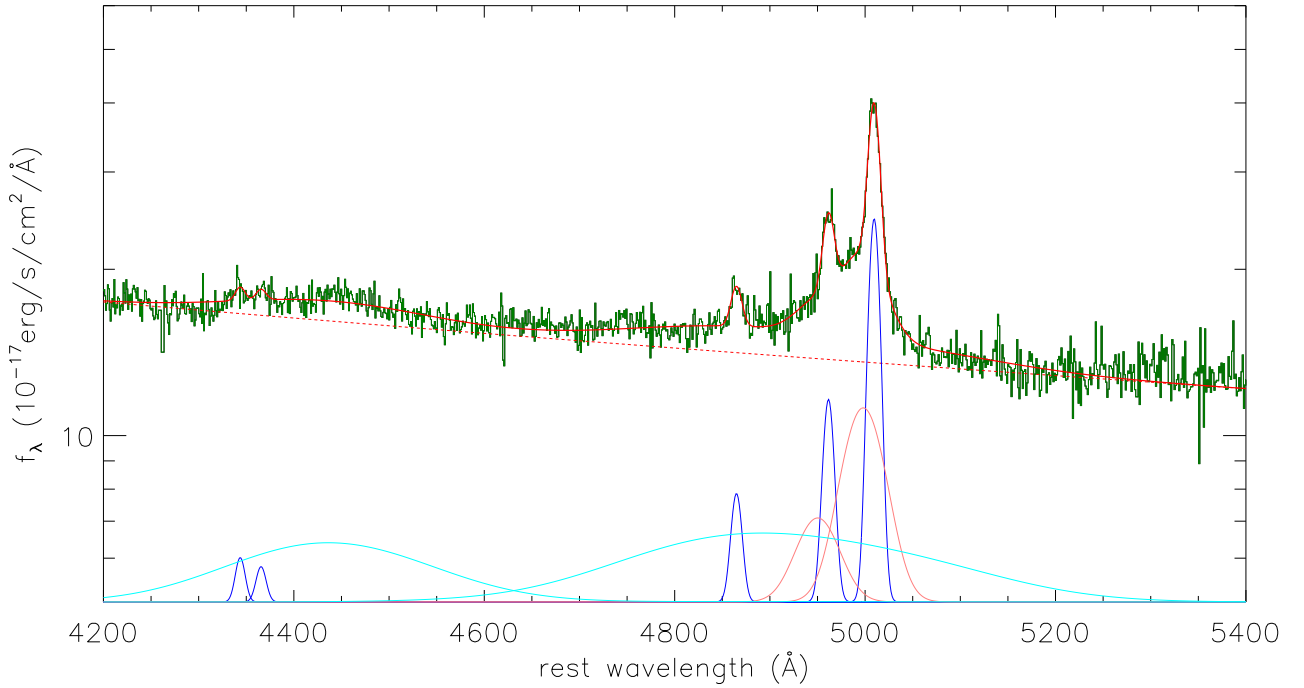


Figure 3. Best-fitting results to the emission lines with rest wavelength from 4200 to 5400Å by model B with considering optical Fe II emissions. Solid dark green line shows the SDSS spectrum, solid red line shows the best-fitting results, dashed red line shows the determined power law continuum emissions, solid blue lines show the determined narrow Balmer line and core components of $[O\ III]$ emissions, solid pink lines show the determined extended components of $[O\ III]$ emissions, solid cyan lines show the determined optical Fe II emissions related to the lower term of the transitions of 4F , 6S in Kovacevic et al. (2010). In order to show clearer results, the Y-axis is in logarithmic coordinate.

to 5400Å are mainly checked, for the emission lines around H β and H γ , by the following three different model functions.

For the model A which assumes the very broad component around 4450Å coming from the Balmer emission regions, the following model functions are included. A narrow plus a broad Gaussian functions (second moment smaller or larger than 500km/s) $G_{H\beta, N}([\lambda_0, \beta_N, \sigma_{\beta_N}, f_{\beta_N}])$ (parameter λ_0 and σ as central wavelength and second moment in units of Å) and $G_{H\beta, B}([\lambda_0, \beta_B, \sigma_{\beta_B}, f_{\beta_B}])$ are applied to describe the H β . A narrow and a broad Gaussian functions $G_{H\gamma, N}([\lambda_0, \gamma_N, \sigma_{\gamma_N}, f_{\gamma_N}])$ and $G_{H\gamma, B}([\lambda_0, \gamma_B, \sigma_{\gamma_B}, f_{\gamma_B}])$ are applied to describe the H γ . Two narrow Gaussian functions $G_{c1}([\lambda_0, c_1, \sigma_{c1}, f_{c1}])$ and $G_{c2}([\lambda_0, c_2, \sigma_{c2}, f_{c2}])$ are applied to describe the core components of the [O III]4959, 5007Å doublet. Two broad Gaussian functions $G_{e1}([\lambda_0, e_1, \sigma_{e1}, f_{e1}])$ and $G_{e2}([\lambda_0, e_2, \sigma_{e2}, f_{e2}])$ are applied to describe the extended components of the [O III] doublet (Greene & Ho 2005a; Shen et al. 2011; Zhang 2021), considering probably spatially extended emission regions for the outflow-related extended [O III] components as discussed in Zakamska et al. (2016). A broad and a narrow Gaussian functions $G_{c3}([\lambda_0, c_3, \sigma_{c3}, f_{c3}])$ and $G_{e3}([\lambda_0, e_3, \sigma_{e3}, f_{e3}])$ are applied to describe the core and the extended components of the [O III]4363Å. A power law component $A \times (\frac{\lambda}{4100\text{Å}})^B$ is applied to describe the continuum emissions underneath the emission lines. When the model functions are applied, the following restrictions are accepted. First, line flux and second moment of each Gaussian component are not smaller than zero. Second, ratios of the central wavelengths (in unit of Å) and second moments (in unit of Å) of $G_{H\beta, N}$ to $G_{H\gamma, N}$ are fixed to be

$$\frac{\lambda_{0, \gamma N}}{4341.68\text{Å}} = \frac{\lambda_{0, \beta N}}{4862.68\text{Å}} \quad \frac{\sigma_{0, \gamma N}}{4341.68\text{Å}} = \frac{\sigma_{0, \beta N}}{4862.68\text{Å}} \quad (1)$$

leading the narrow Balmer lines to have the same redshift and the same line widths. Third, ratios of the central wavelengths, second moments and fluxes of G_{c1} to G_{c2} to G_{c3} are fixed to be

$$\begin{aligned} \frac{\lambda_{0, c1}}{5008.24\text{Å}} &= \frac{\lambda_{0, c2}}{4960.295\text{Å}} = \frac{\lambda_{0, c3}}{4364.436\text{Å}} \\ \frac{\sigma_{0, c1}}{5008.24\text{Å}} &= \frac{\sigma_{0, c2}}{4960.295\text{Å}} = \frac{\sigma_{0, c3}}{4364.436\text{Å}} \\ f_{c1} &= 3 \times f_{c2} \quad (f_{c3} \text{ free}) \end{aligned} \quad (2)$$

Fourth, ratios of the central wavelengths, second moments and fluxes of G_{e1} to G_{e2} to G_{e3} are fixed to be

$$\begin{aligned} \frac{\lambda_{0, e1}}{5008.24\text{Å}} &= \frac{\lambda_{0, e2}}{4960.295\text{Å}} = \frac{\lambda_{0, e3}}{4364.436\text{Å}} \\ \frac{\sigma_{0, e1}}{5008.24\text{Å}} &= \frac{\sigma_{0, e2}}{4960.295\text{Å}} = \frac{\sigma_{0, e3}}{4364.436\text{Å}} \\ f_{e1} &= 3 \times f_{e2} \quad (f_{e3} \text{ free}) \end{aligned} \quad (3)$$

The model parameters of $G_{H\gamma, B}$ and $G_{H\beta, B}$ are free model parameters, which will provide further clues to the origin of the very broad components around 4450Å, from Balmer emissions or from extended [O III] emissions or other physical origins. Then, through the Levenberg-Marquardt least-squares minimization technique, the best-fitting results to the emission lines by the model A can be well determined, and shown in Fig. 2 with $\chi^2/dof \sim 0.88$ (where χ^2 and dof are the summed squared residuals for the best-fitting results and the degree of freedom, respectively). Here, in order to show clearer results, left panel of Fig. 2 shows the best-fitting results to the emission lines around H β with rest wavelength range from 4600 to 5400Å, and right panel of Fig. 2 shows the best-fitting results to the emission lines around H γ with rest wavelength range from 4200 to 4600Å.

Before proceeding further, one point is noted. Besides the two narrow Gaussian components for narrow H β and narrow H γ and two broad Gaussian components for broad H β and broad H γ discussed above, two Gaussian components are also considered in the Model A to describe probable 'outflow components' in narrow H β and narrow H γ (the extended component for wings of narrow Balmer lines, such as the broad Gaussian components included in [O III] lines), and two additional Gaussian components are considered in Model A to describe probable 'outflow components' in broad H β and broad H γ (or to describe probably complicated profiles of broad Balmer lines). However, for the model including the new four additional Gaussian components applied, the determined probable 'outflow components' in broad Balmer lines have fluxes to be zero, and the determined 'outflow components' in narrow Balmer lines have their line fluxes one times smaller than their corresponding uncertainties. Therefore, it is not necessary to consider the probable 'outflow components' in narrow Balmer line or in broad Balmer lines.

The determined parameters of emission lines are listed in Table 1 for the model A. The very broad component around 4450Å can be well described by a broad Gaussian function with central wavelength 4447Å, second moment 42Å, and there is an expected corresponding very broad component underneath of H β described by a broad Gaussian function with central wavelength 4912Å, second moment 95Å. It is clear that the very broad components coming from very extended components of [O III] emissions can be totally ruled out, due to the following main reason. If the very broad component around 4450Å was from extended component of [O III]4363Å, the broad component is a red shifted component, however, for the very component around 4922Å assumed from the extended component of [O III]4959, 5007Å doublet, it is a blue-shifted component. Therefore, the very broad component around 4450Å should be probably from broad Balmer emission lines. However, there are quite different second moments and red-shifted ve-

locities (relative to narrow Balmer lines) of the broad components of $H\beta$ and $H\gamma$, $\sigma_{\beta B} \sim 95\text{\AA}$ ($\sim 5860\text{km/s}$) but $\sigma_{\gamma B} \sim 42\text{\AA}$ ($\sim 2900\text{km/s}$), $\lambda_{0, \beta B} - \lambda_{0, \beta N} \sim 47\text{\AA}$ ($\sim 2900\text{km/s}$) but $\lambda_{0, \gamma B} - \lambda_{0, \gamma N} \sim 104\text{\AA}$ ($\sim 7170\text{km/s}$), leading to incompatible dynamic properties of broad Balmer emission clouds. Moreover, the measured line width of the very broad component around 4450\AA can also be applied to rule out that the determined extended components of $[\text{O III}]\lambda 4959, 5007\text{\AA}$ were actually from broad $H\beta$ emissions, because the extended component has line width about $23\text{--}25\text{\AA}$, 1.9 times smaller than the broad component around 4450\AA . Therefore, the very broad components around 4450\AA and around 4900\AA determined by the Model A are not preferred from broad Balmer emission clouds or from extended $[\text{O III}]$ emission clouds. Preferred choice should be mainly considered for the origin of the very broad components around 4450\AA and around 4910\AA .

For the model B, new model functions are considered as follows. Besides the narrow Balmer emission components and the components from the $[\text{O III}]$ emissions described the Gaussian functions ($G_{H\beta, N}$, $G_{H\gamma, N}$, G_{c1} , G_{c2} , G_{c3} , G_{e1} , G_{e2} , G_{e3}) and the AGN continuum emissions described by a power law function, there is an additional component from optical Fe II emissions described by the broadened optical Fe II template in Kovacevic et al. (2010), which are mainly considered to explain the very broad component around 4450\AA and around 4910\AA . Considering the optical Fe II emission templates in four groups (three groups related to the lower term of the transitions of ^4F , ^6S and ^4G terms, and the fourth group from the I Zw 1 Fe II template) as discussed in Kovacevic et al. (2010), the Fe II component G_{Fe} is described by

$$G_{Fe} = \sum_{i=1}^4 I_i \times T_{Fe, i, V_s, V_b} \quad (4)$$

where $I_i \geq 0$ represents the intensity of Fe II emission features in each group, $T_{Fe, i}$ means the broadened and shifted Fe II emission features in each group, and V_s and V_b means the same shift velocity and the same broadening velocity for the Fe II emission features in the four groups. Then, the same restrictions applied in model A are accepted in model B on the Gaussian components of narrow Balmer emission components and the core and extended components from the $[\text{O III}]$ emissions. Then, through the Levenberg-Marquardt least-squares minimization technique, the best-fitting results to the emission lines by the model B can be well determined after considering the optical Fe II emissions, and shown in Fig. 3 with $\chi_B^2/\text{dof}_B \sim 1330.88/1329$. The determined parameters of emission lines are also listed in Table 1 for the model B. The results by model B are more natural than those by model A, because there is no need to reconcile the contradiction on the origin of the very broad component around 4450\AA and around 4900\AA . Therefore, in the current stage, the model B

is preferred in the SDSS J1058+5443, indicating there are no broad Balmer emission lines in SDSS J1058+5443.

Furthermore, as what we have known that the theoretical flux ratio of $H\beta$ to $H\gamma$ is about 2. The determined flux ratios of narrow $H\beta$ to narrow $H\gamma$ are about $2.70^{+1.98}_{-0.96}$ and $2.78^{+1.09}_{-0.72}$ by model A and by model B, respectively, consistent with the theoretical value, providing further clues to support the reliability of the determined narrow $H\beta$ and narrow $H\gamma$ components by the model A and by the model B.

Moreover, as the shown and determined Fe II emission features by model B in Table 1 and in Fig. 3, Fe II emission features in the two groups related to the lower term of the transitions of ^4F , ^6S in Kovacevic et al. (2010) are strongly apparent, but there are quite weak Fe II emission features related to the groups related to the lower term of the transition of ^4G in Kovacevic et al. (2010) and the Fe II template from I Zw 1. Different intensity ratios of optical Fe II features in the four groups in Kovacevic et al. (2010) can be found in the shown examples in the web-page http://147.91.240.26/FeII_AGN/link6.html maintained by Dr. Kovacevic. And the determined optical Fe II emission features have blue-shifted velocity about -7700km/s and have EW (Equivalent Width) about 64\AA . The blue-shifted velocity is so far the largest blue-shift velocity among the AGN with optical Fe II lines. However, as discussed in Kovacevic et al. (2010) (see their Fig. 17), there is a negative correlation between EW of optical Fe II and EW of $[\text{O III}]\lambda 5007$. In SDSS J1058+5443, the EW 48\AA of $[\text{O III}]\lambda 5007$ and the EW 64\AA of optical Fe II are roughly consistent with the EW correlation between optical Fe II and $[\text{O III}]\lambda 5007$, to provide further clues to support the determined optical Fe II emission features. Furthermore, as discussed above, only Fe II features in two of the four groups in Kovacevic et al. (2010) are strong enough, therefore, the other Fe II templates, such as discussed in Boroson & Green (1992); Veron-Cetty et al. (2004); Tsuzuki et al. (2006), can not efficiently applied to describe the optical features in SDSS J1058+5443, due to partly fixed intensity ratios of optical Fe II features in their templates..

For the model C, based on the results determined by model B, there are two additional broad Gaussian components, $G_{H\beta}([\lambda_{0, \beta}, \sigma_{\beta}, f_{\beta}])$ and $G_{H\gamma}([\lambda_{0, \gamma}, \sigma_{\gamma}, f_{\gamma}])$, in model C applied to describe probable broad Balmer lines, besides the optical Fe II emissions. When, the model C is running, the additional restrictions are accepted on central wavelengths and second moments of $G_{H\beta}$ and $G_{H\gamma}$,

$$\frac{\lambda_{0, \gamma}}{4341.68\text{\AA}} = \frac{\lambda_{0, \beta}}{4862.68\text{\AA}} \quad \frac{\sigma_{0, \gamma}}{4341.68\text{\AA}} = \frac{\sigma_{0, \beta}}{4862.68\text{\AA}} \quad (5)$$

to confirm that the probable broad Balmer lines have the same redshift and the same line widths. Meanwhile, when the model C is running, the determined model parameters of

Table 1. Line parameters of the emission features

Model A				Model B			
Line	λ_0	σ	flux	Line	λ_0	σ	flux
H β_N	4864.56 \pm 0.65	5.45 \pm 0.68	38.29 \pm 4.86	H β_N	4864.91 \pm 0.66	5.79 \pm 0.61	41.23 \pm 4.42
H β_B	4911.72 \pm 11.99	94.66 \pm 9.96	296.69 \pm 42.51
H γ_N	4343.36 \pm 0.58	4.87 \pm 0.61	14.16 \pm 4.96	H γ_N	4343.67 \pm 0.59	5.17 \pm 0.54	14.84 \pm 3.06
H γ_B	4447.14 \pm 3.93	41.67 \pm 4.92	157.07 \pm 19.61
[O III] λ 5007 _c	5009.46 \pm 0.15	5.88 \pm 0.17	288.26 \pm 10.66	[O III] λ 5007 _c	5009.48 \pm 0.15	5.98 \pm 0.16	297.84 \pm 10.11
[O III] λ 5007 _e	4999.51 \pm 1.13	22.25 \pm 1.18	350.95 \pm 19.03	[O III] λ 5007 _e	4996.34 \pm 1.17	22.69 \pm 0.96	357.56 \pm 13.78
[O III] λ 4363 _c	4365.49 \pm 0.13	5.12 \pm 0.15	10.02 \pm 5.22	[O III] λ 4363 _c	4365.52 \pm 0.13	5.21 \pm 0.14	10.53 \pm 2.74
[O III] λ 4363 _e	4356.82 \pm 0.98	19.39 \pm 1.03	34.65 \pm 14.44
...	opt Fe II*	-7702 \pm 256	6200 \pm 400	991 \pm 65

Notice: [O III] λ 5007_c and [O III] λ 5007_e represent the core and the extended component in the [O III] λ 5007Å. [O III] λ 4363_c and [O III] λ 4363_e represent the core and the extended component in the [O III] λ 4363Å. The second and sixth columns show the determined rest central wavelengths in unit of Å (km/s for the shifted velocities of the optical Fe II), the third and seventh columns show the determined line widths (second moment) in unit of Å (the broadening velocity in unit of km/s for the optical Fe II lines), and the fourth and the eighth columns list the determined line flux in the unit of $10^{-17}erg/s/cm^2$. The flux of optical Fe II is total flux of the blue-shifted optical Fe II emissions from 4200Å to 5400Å in SDSS J1058+5443.

the broadening and shift velocities of optical Fe II template are accepted as the starting values in model C, and to assure that the optical Fe II emissions are larger than zero, otherwise, the final results come to be the totally same results as those by model A. Then, through the Levenberg-Marquardt least-squares minimization technique, the best-fitting results to the emission lines by the model C can be well determined after considering the probable broad Balmer lines, with $\chi^2_C/dof_C \sim 1326.69/1325$. The determine broad H β can be describe by a Gaussian component with central wavelength $4890.68 \pm 45.23Å$, second moment $32.69 \pm 41.56Å$, and flux 13.54 ± 21.83 . And the determined broad H γ with line flux zero. The best-fitting results are not shown in plots, but are totally similar as the results shown in Fig. 3, besides the only quite weak broad Gaussian component around 4890.68Å. Based on the determined line flux and line width quite smaller than their corresponding uncertainties of $G_{H\beta}$, the determined broad $G_{H\beta}$ is not reliable enough.

Moreover, the F-test technique can be applied to determine that the broad Gaussian component $G_{H\beta}$ determined by model C is not necessary to be considered. Based on the different χ^2/Dof values for the model C and Model B for optical spectroscopic emissions with and without considerations of probable broad Balmer emission lines, the calculated F_p value is about

$$F_p = \frac{\chi^2_C - \chi^2_B}{dof_C - dof_B} \sim 1.046 \quad (6)$$

Based on $dof_C - dof_B$ and dof_C as number of dofs of the F distribution numerator and denominator, the expected value from the statistical F-test with confidence level about 62% will be near to F_p . Therefore, the confidence level is only about 62%, smaller than 1sigma, to support the broad H β compo-

nent, indicating the determined broad Gaussian component by model C is not preferred.

Therefore, based on the shown and discussed results above, no optical broad emission lines can be preferred in SDSS J1058+5443:

- If there were broad H β and H γ determined by model A, the expected broad H β and broad H γ have significantly different both red-shifted velocities and line widths, leading to incompatible dynamic properties of broad Balmer emission clouds.
- The determined extended components of [O III] doublet are truly from [O III] emissions, not part of broad H β emissions.
- Considering blue-shifted optical Fe II emissions, optical spectroscopic emission features can be naturally described.
- The F-test technique can be well applied to confirm that it is not necessary to consider broad Balmer lines, once the optical Fe II emissions are fully considered.

2.2. Properties of NUV Mg II line

Besides properties of the optical Balmer emission lines, emission lines around Mg II with rest wavelength range from 2600 to 3600Å can be well measured by two different models as follows. Here, the selected wavelength range extending to 3600Å can lead to well determined continuum emissions.

In model A, a broadened and shifted UV Fe II template discussed in Kovacevic-Dojcinovic & Popovic (2015) plus a broad Gaussian function and a power law component are applied to describe the emissions. Here, considering the UV Fe II templates in four groups (4 multiplets: 60 within

2907 to 2979Å, 61 within 2861 to 2917Å, and 62 and 63 which overlap within 2709 to 2749Å) as discussed in Kovacevic-Dojcinovic & Popovic (2015), the UV Fe II component G_{uFe} is described by

$$G_{uFe} = \sum_{i=1}^4 I_i \times T_{uFe, i, V_{us}, V_{ub}} \quad (7)$$

where $I_i \geq 0$ represents the intensity of UV Fe II emission features in each group, $T_{uFe, i}$ means the broadened and shifted UV Fe II emission features in each group, and V_{us} and V_{ub} means the same shifted velocity and the same broadening velocity for the UV Fe II emission features in the four groups. The best-fitting results are shown in the left panel of Fig 4 with $\chi_A^2/dof_A \sim 1345.73/1442 \sim 0.93$ by model A. The determined broad Mg II has the central wavelength $2803.61 \pm 13.48\text{Å}$, second moment $43.86 \pm 25.82\text{Å}$ ($\sim 4700\text{km/s}$), and line flux $(355.01 \pm 531.71) \times 10^{-17} \text{erg/s/cm}^2$. Considering the measured line flux smaller than the corresponding uncertainty, the determined broad Mg II component is not reliable enough. The measured broadening velocity and blue-shifted velocity of the UV Fe II emissions are about $5888 \pm 965\text{km/s}$ and $-12820 \pm 1376\text{km/s}$. And, the UV Fe II emission features in the two groups from multiplets 60 and 62 are more strongly apparent than the features from the multiplets 61 and 63.

In model B with no considerations of broad Mg II component, only the broadened and shifted UV Fe II template discussed in Kovacevic-Dojcinovic & Popovic (2015) plus a power law component are applied to describe the emissions lines. The best-fitting results are shown in right panel of Fig 4 with $\chi_B^2/dof_B \sim 1347.47/1445 \sim 0.93$ by model B. The measured broadening velocity and blue-shifted velocity of the UV Fe II emissions are about $6757 \pm 239\text{km/s}$ and $-14140 \pm 1155\text{km/s}$. And, the UV Fe II emission features in the two groups from multiplets 60 and 62 are more strongly apparent than the features from the multiplets 61 and 63. Meanwhile, if the UV Fe II components including apparent effects of central radial flows, the larger blue-shifted velocity in UV Fe II emissions than in optical Fe II emissions can be well accepted, after accepted UV Fe II emissions are from regions nearer to central power source. Model B not considering a broad Gaussian component can also lead to well accepted best-fitting results to the emission lines around 2800Å.

Not only the large uncertainties of line flux and second moments as clues to rule out the expected broad Mg II component, the F-test technique can be also applied to determine that the broad Gaussian component is not necessary to be considered. Based on the different χ^2/Dof values for the model A and Model B for emission lines around 2800Å, the

calculated F_p value is about

$$F_p = \frac{\chi_A^2 - \chi_B^2}{dof_A - dof_B} \sim 0.62 \quad (8)$$

Based on $dof_A - dof_B$ and dof_A as number of dofs of the F distribution numerator and denominator, the expected value from the statistical F-test with confidence level about 40% will be near to F_p . Therefore, the confidence level is only about 40%, smaller than 1sigma, to support the broad Mg II component, indicating the determined broad Gaussian component by model A is not preferred. Certainly, the discussed results above are only based on different model functions and corresponding F-test technique, further efforts are necessary to totally confirm the discussed results above.

Furthermore, as discussed in Kovacevic-Dojcinovic & Popovic (2015) (see left panel in their Fig. 10), there is one positive broadening velocity correlation between optical Fe II emission features and UV Fe II features. Based on the determined broadening velocity about 6700km/s of UV Fe II emission features and the determined broadening velocity about 6200km/s of optical Fe II emission features in SDSS J1058+5443, there are clues to consider SDSS J1058+5443 to simply follow the broadening velocity correlation between UV and optical Fe II emission features.

3. BH MASS OF SDSS J1058+5443

BH mass, one of fundamental parameters of AGN, is mainly estimated in the subsection. BH mass properties will be used in the following subsections to provide further clues to confirm probable loss of central BLRs in SDSS J1058+5443. Due to no apparent broad emission lines in SDSS J1058+5443, the reported virial BH mass is not considered in the manuscript based on the Virialization assumption applied to broad line emission clouds (Peterson et al. 2004; Shen et al. 2011). The following two methods are mainly considered.

First, based on the dependence of BH masses on continuum luminosity reported in Equation (9) in Peterson et al. (2004), BH mass of SDSS J1058+5443 can be estimated as

$$M_{BH} \propto (\lambda L_{5100})^{0.79 \pm 0.09} \sim 3.02_{-0.84}^{+1.17} \times 10^8 M_\odot \quad (9)$$

with BH mass uncertainty determined by uncertainty of continuum luminosity and uncertainties of the factors in the equation.

Second, the commonly accepted AGNSPEC code (Hubeny et al. 2000; Davis et al. 2007) is applied to roughly determine the central BH mass through properties of spectral energy distributions of SDSS J1058+5443, considering the non-LTE general relativistic accretion disk models. Fig. 5 shows the best descriptions to the SDSS spectrum of SDSS J1058+5443 with emission line features around 2800Å (from 2700Å to 2950Å) and around

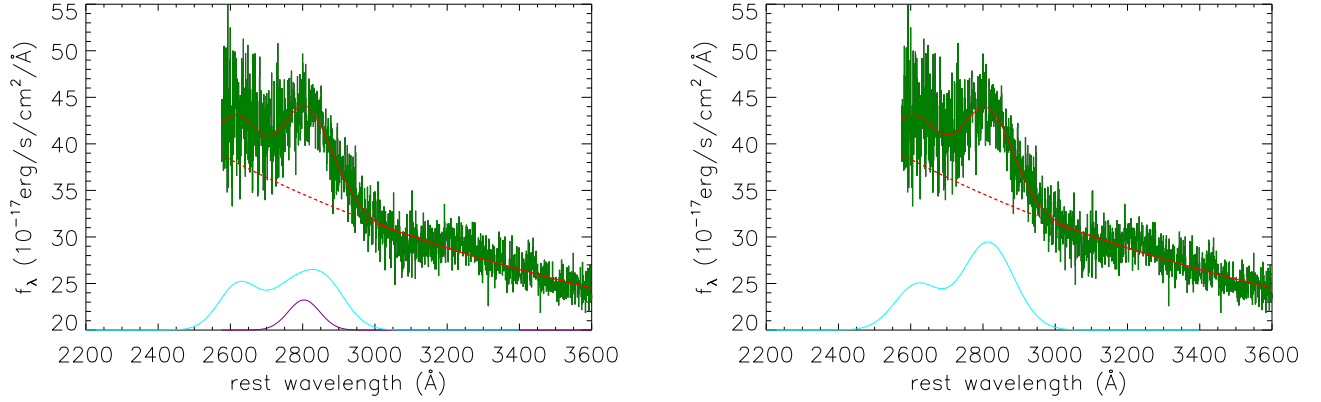


Figure 4. Best fitting results to the emissions around 2800Å by Model A (left panel) and model B (right panel). In each panel, solid dark green line shows the SDSS spectrum, solid red line shows the best-fitting results, dashed red line shows the determined power law continuum emissions, solid cyan line shows the determined UV Fe II emissions. In left panel, solid purple line shows the determined broad Gaussian component of Mg II by model A.

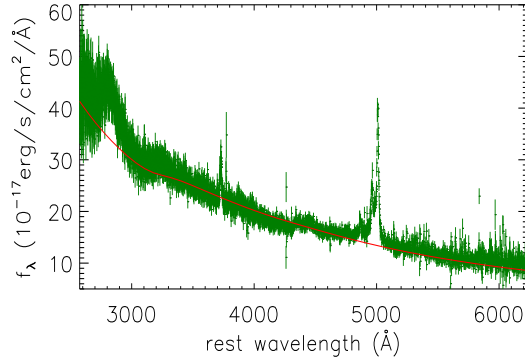


Figure 5. The best descriptions to the SDSS continuum emissions through the well applied AGNSPEC code. Dots plus error bars in dark green show the SDSS spectrum, solid red line shows the determined best descriptions to continuum emissions.

4900Å (from 4800Å to 5100Å) being masked out, with the BH mass $M_{BH} \sim (2.5 \pm 1.1) \times 10^8 M_\odot$, accretion rate $\dot{M} \sim 0.03 \pm 0.01 M_\odot/\text{year}$, BH spin $a_* \sim 0.91 \pm 0.06$, and inclination angle $\cos(i) \sim 0.32 \pm 0.11$, through the AGNSPEC code created templates applied through the Levenberg-Marquardt least-squares minimization technique.

The two different methods lead to similar BH mass, therefore the mean value $M_{BH} \sim (2.8 \pm 1.4) \times 10^8 M_\odot$ is accepted as the BH mass of SDSS J1058+5443 in the manuscript¹.

4. MAIN DISCUSSIONS

4.1. Re-constructed probable intrinsic but hidden broad Balmer lines?

Based on the estimated BH mass, the intrinsic broad Balmer lines could be re-constructed. Then, it is interesting to check whether the expected intrinsic broad Balmer lines are actually overwhelmed in noises of SDSS spectrum of SDSS J1058+5443.

Not similar as the previous reported candidates of true type-2 AGN, weak broad emission components could lead to none detected broad emission lines in low quality spectra with large noises. In the blue quasar SDSS J1058+5443, strong power law AGN continuum emissions clearly indicate strong intrinsic broad Balmer emission lines, if there were broad line emissions. Based on the strong positive linear correlation (scatter of 0.2dex) between AGN continuum luminosity and total Balmer line luminosity from SDSS quasars in

¹The virial BH mass about $3 \times 10^9 M_\odot$ is reported in Shen et al. (2011) in SDSS J1058+5443. However, as discussed above, the virial BH mass sensitively depending on broad line properties should be not reliable enough in SDSS J1058+5443. Therefore, rather than the virial BH mass $3 \times 10^9 M_\odot$, the mass $M_{BH} \sim 2.8 \times 10^8 M_\odot$ is accepted in SDSS J1058+5443 in the manuscript. Moreover, after checked the results in Shen et al. (2011), there is weak correlation between virial BH mass and narrow line width in SDSS quasars, with Spearman rank correlation coefficient only about 0.07. Therefore, in the manuscript, we do not consider line width (second moment) $350 \pm 15 \text{ km/s}$ of core component of [O III] $\lambda 5007\text{Å}$ to be accepted as substitute of stellar velocity dispersion, and then to estimate BH mass by the M-sigma relation (Ferrarese & Merritt 2000; Gebhardt et al. 2000; Kormendy & Ho 2013; McConnell & Ma 2013; Bennert et al. 2015; Savorgnan & Graham 2015; Batista et al. 2017).

Greene & Ho (2005), the expected total $H\beta$ luminosity (including both the broad and the narrow components in $H\beta$) of SDSS J1058+5443 could be

$$L(H\beta) \propto (\lambda L_{5100})^{1.133} \sim (1.02 \pm 0.48) \times 10^{43} \text{ erg/s} \quad (10)$$

with uncertainty $0.48 \times 10^{43} \text{ erg/s}$ determined by the accepted scatter of 0.2dex of the correlation above. Considering the measured line luminosity of narrow $H\beta$ about $(3.57 \pm 0.38) \times 10^{41} \text{ erg/s}$ of SDSS J1058+5443, the expected broad $H\beta$ luminosity (the total $H\beta$ luminosity minus the narrow $H\beta$ luminosity) should be about $(9.84 \pm 4.82) \times 10^{42} \text{ erg/s}$, the corresponding broad $H\beta$ line flux is $(1132 \pm 550) \times 10^{-17} \text{ erg/s/cm}^2$, about 27 times stronger than the narrow $H\beta$ in SDSS J1058+5443. And due to the strong blue quasar-shape continuum emissions in SDSS J1058+5443, there are no obscurations considered on the line flux of emission lines.

If the expected broad $H\beta$ with line luminosity of $(9.84 \pm 0.24) \times 10^{42} \text{ erg/s}$ was intrinsically true in SDSS J1058+5443, there was only one point leading the expected strong broad $H\beta$ not to be detected in the SDSS spectrum: the strong broad $H\beta$ was extremely broad enough that the expected broad $H\beta$ with very lower heights are totally overwhelmed by the noises of SDSS spectrum. However, considering the estimated BH mass $M_{BH} \sim (2.8 \pm 1.4) \times 10^8 M_\odot$, line width σ_B of the expected intrinsic broad Balmer lines can be well estimated through the Virialization assumption (Peterson et al. 2004) combining with size-luminosity empirical relation (Bentz et al. 2013) (scatter of 0.13dex) to estimate distance R_{BLRs} of BLRs to central BH,

$$R_{BLRs} \propto L_{5100}^{0.542} \sim 93 \pm 28 \text{ light-days} \quad (11)$$

$$\sigma_B(H\beta) = \left(\frac{G M_{BH}}{5.5 R_{BLRs}} \right)^{0.5} \sim 1700 \pm 700 \text{ km/s}$$

where the factor 5.5 is the applied scale factor to estimate Virial BH mass used in Peterson et al. (2004), and uncertainty 28light-days of R_{BLRs} is determined by the scatter of 0.13dex of the size-luminosity empirical relation, and uncertainty 700km/s of $\sigma_B(H\beta)$ is determined by the uncertainties of both BH mass and R_{BLRs} . Based on second moment $\sigma_B(H\beta) = 1700 \pm 700 \text{ km/s}$ and line flux $f_B(H\beta) = (1132 \pm 550) \times 10^{-17} \text{ erg/s/cm}^2$, the expected intrinsic Gaussian-like broad $H\beta$ $G_{H\beta}$, $N([\lambda_0, \sigma_B(H\beta), f_B(H\beta)])$ with central wavelength $\lambda_0 = 4862 \text{ \AA}$ can be well re-constructed and shown in Fig. 6, after considering uncertainties of parameters of $\sigma_B(H\beta)$ and $f_B(H\beta)$. It is clear that the expected intrinsic broad $H\beta$ is strong enough, if there was, the intrinsic broad $H\beta$ can not be overwhelmed by noises of SDSS spectrum.

4.2. Re-constructed probable intrinsic but hidden broad Mg II line?

Similar as the procedure to re-construct intrinsic broad $H\beta$ (if there was), the intrinsic broad Mg II can also be re-constructed, to check whether the intrinsic broad Mg II line

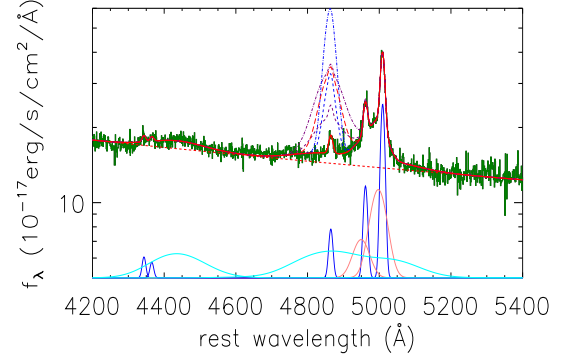


Figure 6. The expected intrinsic broad $H\beta$ through the properties of virial BH mass in SDSS J1058+5443. Symbols and line styles have the same meanings as those shown in Fig. 3, but the dashed red line, dot-dashed purple line, dashed purple line, dot-dashed blue line and dashed blue line show the re-constructed $H\beta$ after considering the intrinsic broad $H\beta$ emission features (if there were) with Gaussian parameters $[\lambda_0/\text{\AA}, \sigma_B(H\beta)/(\text{km/s}), f_B(H\beta)/(10^{-17} \text{ erg/s/cm}^2)]$ as $[4862, 1700, 1132]$, $[4862, 1700+700, 1132+550]$, $[4862, 1700+700, 1132-550]$, $[4862, 1700-700, 1132+550]$, $[4862, 1700-700, 1132-550]$, respectively.

can be hidden or overwhelmed in the noises of SDSS spectrum, if there was intrinsic broad Mg II line.

First, based on the strong positive linear correlation (scatter of 0.15dex) between AGN continuum luminosity at 3000 \AA and Mg II line luminosity from SDSS quasars in Shen et al. (2011) and the measured continuum luminosity at 3000 \AA about $L_{3000} \sim (8.95 \pm 0.55) \times 10^{44} \text{ erg/s}$ in SDSS J1058+5443, the expected Mg II line luminosity of SDSS J1058+5443 could be

$$L(Mg) \propto (\lambda L_{3000})^{0.909} \sim (1.11 \pm 0.43) \times 10^{43} \text{ erg/s} \quad (12)$$

with uncertainty $0.43 \times 10^{43} \text{ erg/s}$ determined by the accepted scatter of 0.15dex of the correlation above, leading the corresponding broad Mg II line flux to be $(1280 \pm 490) \times 10^{-17} \text{ erg/s/cm}^2$.

Second, accepted the Virialization assumption to broad Mg II emission clouds as discussed in Shen et al. (2011), the line width (FWHM, full width at half maximum) can be estimated as

$$FWHM(Mg) = \left(\frac{M_{BH}}{5.5 \left(\frac{L_{3000}}{10^{44} \text{ erg/s}} \right)^{0.62}} \right)^{0.5} \sim 3750 \pm 950 \text{ km/s} \quad (13)$$

with uncertainty 950km/s of $FWHM(Mg)$ determined by the uncertainties of both BH mass and L_{3000} , leading to second moment about $1590 \pm 400 \text{ km/s}$ assuming a Gaussian broad Mg II line. Then, based on second moment $\sigma(Mg) = 1590 \pm 400 \text{ km/s}$ and line flux $f(Mg) = (1280 \pm 490) \times 10^{-17} \text{ erg/s/cm}^2$ and assumed central wavelength 2800 \AA , the

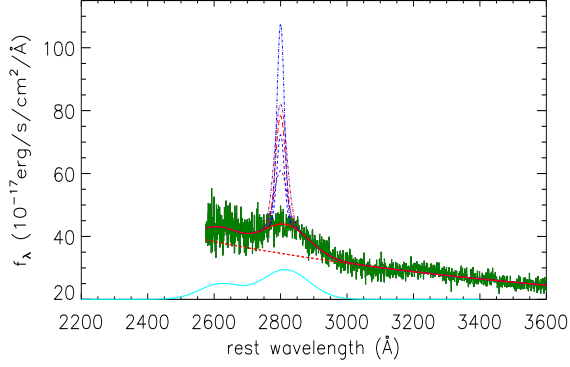


Figure 7. The expected intrinsic broad Mg II through the properties of virial BH mass in SDSS J1058+5443. Symbols and line styles have the same meanings as those shown in right panel of Fig. 4, but the dashed red line, dot-dashed purple line, dashed purple line, dot-dashed blue line and dashed blue line show the re-constructed intrinsic broad Mg II emission features (if there were) after considering the intrinsic broad Mg II emission features (if there were) with Gaussian parameters $[\lambda_0/\text{\AA}, \sigma(Mg)/(\text{km/s}), f(Mg)/(10^{-17}\text{erg/s/cm}^2)]$ as [2800, 1590, 1280], [2800, 1590+400, 1280+490], [2800, 1590+400, 1280-490], [2800, 1590-400, 1280+490], [2800, 1590-400, 1280-490], respectively.

expected intrinsic Gaussian-like broad Mg II can be well re-constructed and shown in Fig. 7, after considering uncertainties of parameters of $\sigma(Mg)$ and $f(Mg)$. It is clear that the expected intrinsic broad Mg II is strong enough, if there was, the intrinsic broad Mg II cannot be overwhelmed by noises of SDSS spectrum.

Now, based on the re-constructed broad Balmer lines and Mg II line, if there were intrinsic broad emission lines, it is interesting to compare the expected SDSS spectrum of SDSS J1058+5443 considering the probable intrinsic broad lines and the composite spectrum of SDSS quasars. The comparison is shown in Fig. 8. Here, the expected intrinsic broad H γ and H δ are re-constructed based on the re-constructed broad H β with line flux ratios to be $f_{4862} : f_{4341} : f_{4103} = 1 : 0.5 : 0.3$ ($f_{4862} = 1132 \times 10^{-17}\text{erg/s/cm}^2$) and with the same line width (1700km/s) in velocity space and with the same redshift. It is clear that the spectroscopic features with considering the expected intrinsic broad lines are totally similar as those of composite spectrum of SDSS quasars. In one word, if there were intrinsic broad lines, the broad lines cannot be hidden or overwhelmed in noises of SDSS spectrum in SDSS J1058+5443. Therefore, it can be clearly confirmed the loss of broad lines in the SDSS J1058+5443.

4.3. Further discussions

Besides the detailed discussions on emission lines, origin of blue continuum emissions is simply considered in the subsection, in order to confirm that SDSS J1058+5443 is truly an AGN.

There are two further points applied to confirm that the blue continuum emissions are not from younger stellar objects but from the central AGN activities in SDSS J1058+5443. On the one hand, long-term variabilities of SDSS J1058+5443 is well checked through the collected 8years-long light curve from the CSS (the Catalina Sky Survey) (Drake et al. 2009) shown in Fig. 9. The apparent variabilities can be well described by the Damped Random Walk (DRW) process (Kelly et al. 2009; Kozłowski et al. 2010; Zu et al. 2013) which has been proved to be the preferred process to describe intrinsic AGN variabilities. Through the public code of JAVELIN, the determined DRW process parameter of the characteristic variability timescale is about $\ln(\tau/\text{days}) \sim 4.95 \pm 0.54$ ($\tau \sim 140\text{days}$), similar as the mean value of τ in SDSS quasars well discussed in MacLeod et al. (2010). On the other hand, the determined flux ratio of the total [O III] $\lambda 5007\text{\AA}$ (both the core and broad component) to the narrow H β is about 16.3 larger than 10, indicating strong central AGN activities in SDSS J1058+5443 by applications of BPT diagrams (Kewley et al. 2019; Zhang et al. 2020). Therefore, the apparently blue continuum emissions are confirmed to be from central AGN activities. And then, due to the strong blue continuum emissions from central AGN activities, there are no discussions on the loss of broad emission lines due to SDSS J1058+5443 classified as a changing-look AGN at dim state (Tohline & Osterbrock 1976; LaMassa et al. 2015; Yang et al. 2018; Zhang 2021b).

Moreover, the none detected broad emission lines are not due to SDSS J1058+5443 as a BL Lac (Plotkin et al. 2008). The radio properties of SDSS J1058+5443 is well checked through the Faint Images of the Radio Sky at Twenty-cm (FIRST) (Helfand et al. 2015). The radio intensity at 1.4GHz is about 17.7mJy in SDSS J1058+5443, leading SDSS J1058+5443 to be a radio loud AGN with radio loudness about 29. However, the [O III] $\lambda 5007\text{\AA}$ has rest equivalent width (EW) about 49 \AA very larger than 5 \AA , indicating SDSS J1058+5443 is not a BL Lac object but a normal radio loud quasar.

4.4. What should be done in the near future?

Actually, there is one surefire way to confirm the SDSS J1058+5443 as a true type-2 AGN. To get the spectroscopic observations around H α will provide robust evidence to support the conclusions in the manuscript for SDSS J1058+5443. If there were no broad components of H α , there will be no doubt to well identify the SDSS J1058+5443 as a true type-2 AGN. We wish there will be good chance to get NIR spectroscopic observations of the SDSS J1058+5443 in the near future.

4.5. Physical origin of the loss of central normal BLRs in SDSS J1058+5443

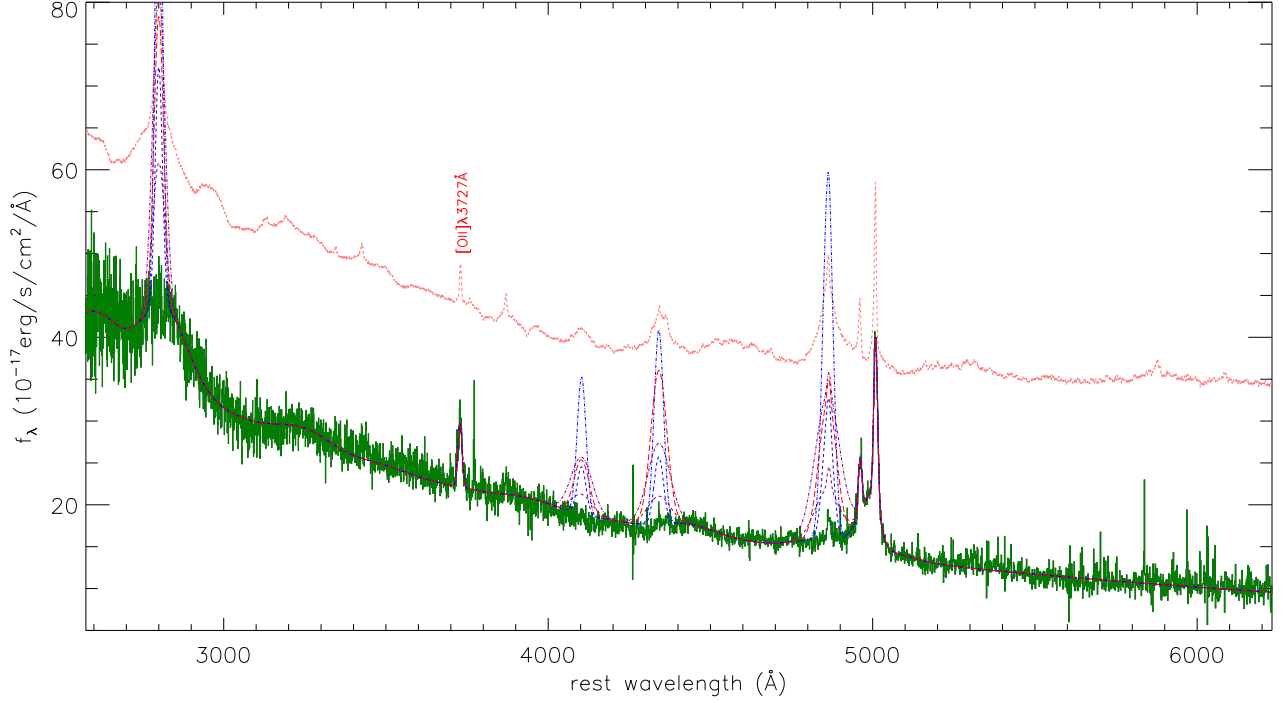


Figure 8. The comparison between composite spectrum of SDSS quasars and the spectrum of SDSS J1058+5443 considering the probable intrinsic broad lines (if there were) under the Virialization assumption applied to broad line clouds. Dashed pink line shows the composite spectrum of SDSS quasars, solid dark green line shows the SDSS spectrum of SDSS J1058+5443. Solid red lines around 5000Å and around 3727Å show the best descriptions to the [O III]λ4959, 5007Å and [O II]λ3727Å emission lines. Around 4861Å, 4341Å, 4103Å and 2800Å, dashed red lines, dot-dashed purple lines, dashed purple lines, dot-dashed blue lines and dashed blue line show the re-constructed intrinsic broad lines (if there were), after considering uncertainties of line widths and line fluxes, similar as shown in Fig. 6 and in Fig. 7.

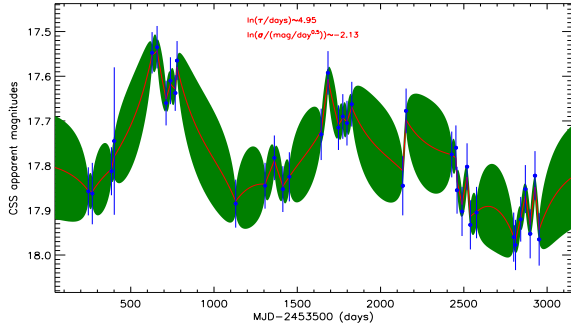


Figure 9. Long-term variabilities of SDSS J1058+5443 from the CSS. Solid circles plus error bars in blue show the collected data points from the CSS, solid red line and the area covered by light green show the best descriptions and the corresponding 1sigma confidence bands to the light curve by the JAVELIN code. The determined characteristic variability timescale and amplitude are marked in the top corner.

Once loss of broad emission lines can be confirmed, it is interesting to consider the potential physical origin of the loss of central normal BLRs. In SDSS J1058+5443 with bolometric luminosity about $6 - 9 \times 10^{45}$ erg/s (about 10 times of the continuum luminosity λL_{5100}) (Netzer 2019), both the steep

bluer power law AGN continuum emissions and the strong bolometric luminosity indicate that the disk-wind scenario with luminosities higher than 10^{46} erg/s as well discussed in Elitzur & Netzer (2016) can be well applied to explain the loss of broad emission lines in SDSS J1058+5443, rather than the accreting process with lower accretion rates as discussed in Cao (2010); Nicastro et al. (2003); Elitzur & Ho (2009), etc. And the apparent blue-shifted broad UV and OPT Fe II emission lines and the AGNSPEC simply determined large $a_* \sim 0.91$ can provide probable clues to support the expected disk-winds scenario in Elitzur & Netzer (2016).

Before the end of the subsection, one point should be noted. As discussed in Villar Martin et al. (2020), there is a special subclass of AGN, the called core-extremely red quasars (core-ERQs) previously defined in Hamann et al. (2017), representing an intermediate evolutionary phase in which a heavily obscured quasar is blowing out the circumnuclear interstellar medium, leading to commonly consequent extreme outflows in high luminosity core-ERQs. In other words, the conditions of the disk-wind scenario discussed in Elitzur & Netzer (2016) could be well satisfied in high luminosity core-ERQs, however, there are common BLRs in core-ERQs. Therefore, the proposed disk-wind scenario dis-

cussed in [Elitzur & Netzer \(2016\)](#) can be applied to explain the disappearance of central BLRs, but cannot be accepted as a standard criterion leading to disappearance of central BLRs in AGN.

5. SUMMARIES AND CONCLUSIONS

Finally, the main conclusions are given as follows.

- SDSS J1058+5443 is a blue quasar with apparently blue continuum emissions coming from central AGN activities, based on DRW process well determined long-term variabilities and flux ratio larger than 10 of [O III] to narrow $H\beta$ of SDSS J1058+5443. Not similar as previous reported candidates of true type-2 AGN among emission-line objects with weak AGN activities but strong host galaxy contribution, properties of SDSS J1058+5443 could provide more robust evidence to support the very existence of true type-2 AGN.
- Considering different model functions applied to describe emission lines around $H\beta$, rather than broad Balmer lines but blue-shifted optical Fe II emissions can be preferred in SDSS J1058+5443, leading to the conclusion that there are no broad optical Balmer emission lines in SDSS J1058+5443. The confidence level is smaller than 1sigma to support probably existence of broad Balmer emission lines.
- Considering different model functions applied to describe emission lines around 2800Å in SDSS J1058+5443, the blue-shifted UV Fe II emissions can be preferred in SDSS J1058+5443, leading to the conclusion that there are no broad NUV Mg II line in SDSS J1058+5443. The confidence level is smaller than 1sigma to support probably existence of broad NUV Mg II line.
- Considering Virialization assumption to broad emission clouds in SDSS J1058+5443, combining with estimated BH mass, the expected intrinsic broad opti-

cal Balmer lines and NUV Mg II line can be well reconstructed, if there were intrinsic broad emission lines in SDSS J1058+5443. The SDSS spectrum plus reconstructed broad lines are totally similar as the composite spectrum of SDSS quasars.

- The re-constructed intrinsic broad lines can not be hidden or overwhelmed in the noises of SDSS spectrum of SDSS J1058+5443, indicating the loss of broad emission lines are not due to spectral quality.
- The SDSS J1058+5443 is so far the best candidate of true type-2 quasar, leading to the clear answer to the very existence of true type-2 AGN. And the expected disk-winds scenario with high luminosity could be preferred to explain the loss of central BLRs in SDSS J1058+5443.

ACKNOWLEDGEMENTS

Zhang and Zhao gratefully acknowledge the anonymous referee for giving us constructive comments and suggestions to greatly improve our paper. Zhang gratefully acknowledges the financial support of NSFC-12173020. The manuscript has made use of the data from the SDSS (<https://www.sdss.org/>) funded by the Alfred P. Sloan Foundation, the Participating Institutions, the National Science Foundation and the U.S. Department of Energy Office of Science. The manuscript has made use of the long-term variability data from the CSS (<http://nesssi.cacr.caltech.edu/DataRelease/>). The manuscript has made use of the NASA/IPAC Extragalactic Database (NED) (<http://ned.ipac.caltech.edu/classic/>). The manuscript has made use of the VLA FIRST Survey (<http://sundog.stsci.edu/>). The manuscript has made use of the public JAVELIN code to describe long-term intrinsic variability properties of AGN (<http://astro.sjtu.edu.cn/~yingzu/codes.html>). The manuscript has made use of the AGNSPEC code to describe SEDs from accretion disks around central black holes (https://github.com/jhmatthews/agnspec_grids).

REFERENCES

- Antonucci, R., 1993, *ARA&A*, 31, 473
- Antonucci, R. J.; Miller, J. S. 1985, *ApJ*, 297, 621
- Avni, Y., 1976, *ApJ*, 210, 642
- Barth, A. J.; Voevodkin, A.; Carson, D. J.; Wozniak, P., 2014, *ApJ*, 147, 12
- Batiste, M.; Bentz, M. C.; Raimundo, S. I.; Vestergaard, M.; Onken, C. A., 2017, *ApJL*, 838, 10
- Bennert, V. N., et al., 2015, *ApJ*, 809, 20
- Bentz, M. C.; Denney, K. D.; Grier, C. J.; et al., 2013, *ApJ*, 767, 149
- Bianchi S., et al., 2012, *MNRAS*, 426, 3225
- Bianchi, S.; Antonucci, R.; Capetti, A; et al., 2019, *MNRAS Letter*, 488, 1
- Boroson, T. A., Green, R. F. 1992, *ApJS*, 80, 10
- Brotherton, M. S.; Singh, V.; Runnoe, J., 2015, *MNRAS*, 454, 3864
- Cao, X. W., 2010, *ApJ*, 724, 855
- Cardamone, C. N.; Moran, E. C.; Kay, L. E., 2007, *AJ*, 134, 1263
- Diamond-Stanic, A. M.; Fan, X.; Brandt, W. N.; et al., 2009, *ApJ*, 699, 782

- Davis, S. W.; Woo, J.; Blaes, O. M., 2007, *ApJ*, 668, 682
- D'Abrusco, R.; Alvarez Crespo, N.; Massaro, F.; et al., 2019, *ApJS*, 242, 4
- Drake, A. J.; Djorgovski, S. G.; Mahabal, A.; et al., 2009, *ApJ*, 696, 870
- Elitzur, M.; Ho, L. C., 2009, *ApJL*, 701, 90
- Elitzur, M.; Netzer, H., 2016, *MNRAS*, 495, 585
- Foreman-Mackey, D.; Hogg, D. W.; Lang, D.; Goodman, J., 2013, *PASP*, 125, 306
- Ferrarese, F.; Merritt, D., 2000, *ApJL*, 539, 9
- Gebhardt, K., et al., 2000, *ApJL*, 539, 13
- Greene, J. E.; Ho, L. C., 2005a, *ApJ*, 627, 721
- Greene, J. E.; Ho, L. C., 2005, *ApJ*, 630, 122
- Hamann, F.; Zakamska, N.L.; Ross, N., et al. 2017, *MNRAS*, 464, 3431
- Helfand, D. J.; White, R. L.; Becker, R. H., 2015, *ApJ*, 801, 26
- Hubeny, I.; Agol, E.; Blaes, O.; Krolik, J. H., 2000, *ApJ*, 533, 710
- Ichikawa, K.; Packham, C.; Ramos A., C.; et al., 2015, *ApJ*, 803, 57
- Kelly, B. C.; Bechtold, J.; Siemiginowska, A., 2009, *ApJ*, 698, 895
- Kewley, L. J.; Nicholls, D. C.; Sutherland, R. S., 2019, *ARA&A*, 57, 511
- Kormendy, J.; Ho, L. C., 2013, *ARA&A*, 51, 511
- Kovacevic-Dojcinovic, J.; Popovic, L. C., 2015, *ApJS*, 221, 35
- Kovacevic, J.; Popovic, L. C.; Dimitrijevic, M. S., 2010, *ApJS*, 189, 15
- Kozlowski, S., et al., 2010, *ApJ*, 708, 927
- LaMassa, S. M.; Cales, S.; Moran, E. C., et al. 2015, *ApJ*, 800, 144
- Li, Y.; Yuan, W.; Zhou, H. Y.; Komossa, S.; Ai, Y. L.; Liu, W. J.; Boisvert, J. H., 2015, *ApJ*, 149, 75
- MacLeod, C. L.; Ivezić, Z.; Kochanek, C. S.; et al., 2010, *ApJ*, 721, 1014
- Marculewicz, M.; Nikolajuk, M., 2020, *ApJ*, 897, 117
- Marlar, A.; Shemmer, O.; Anderson, S. F.; et al., 2018, *ApJ*, 865, 92
- McMahon, R. G.; White, R. L.; Helfand, D. J.; Becker, R. H., 2002, *ApJS*, 143, 1
- McConnell, N. J.; Ma, C. P., 2013, *ApJ*, 764, 184
- Nagao, T.; Kawabata, K. S.; Murayama, T.; Ohyama, Y.; Taniguchi, Y.; Sumiya, R.; Sasaki, S. S., 2004, *ApJ*, 128, 109
- Netzer, H., 2019, *MNRAS*, 488, 5185
- Nicastro, F.; Martocchia, A.; Matt, G., 2003, *ApJ*, 589, L13
- Netzer, H., 2015, *ARA&A*, 53, 365
- Paul, J. D.; Plotkin, R. M.; Shemmer, O.; et al., 2022, *ApJ*, 929, 78
- Peterson, B. M.; Ferrarese, L.; Gilbert, K. M.; et al., 2004, *ApJ*, 613, 682
- Plotkin, R. M.; Anderson, S. F.; Patrick, B.; Hall, P. B.; et al., 2008, *AJ*, 135, 2453
- Plotkin, Richard M.; Shemmer, Ohad; Trakhtenbrot, B.; et al., 2015, *ApJ*, 805, 123
- Pons, E.; Watson, M. G., 2016, *A&A*, 594, 72
- Savic, D.; Goosmann, R.; Popovic, L. C.; Marin, F.; Afanasiev, V. L., 2018, *A&A*, 614, 120
- Savorgnan, G. A. D.; Graham, A. W., 2015, *MNRAS*, 446, 2330
- Shemmer, O.; Trakhtenbrot, B.; Anderson, S. F.; et al., 2010, *ApJL*, 722, 152
- Shen, Y.; Richards, G. T.; Strauss, M., et al., 2011, *ApJS*, 194, 45
- Shi, Y.; Rieke, G. H.; Smith, P.; et al., 2010, *ApJ*, 714, 115
- Tran, H. D., 2001, *ApJL*, 554, 19
- Tran, H. D., 2003, *ApJ*, 583, 632
- Tohline, J. E.; Osterbrock, D. E. 1976, *ApJL*, 210, L117
- Tsuzuki, Y.; Kawara, K.; Yoshii, Y.; Oyabu, S.; Tanabe, T.; Matsuoka, Y., 2006, *ApJ*, 650, 57
- Vanden Berk, D. E., et al., 2001, *AJ*, 122, 549
- Veron-Cetty, M. -P.; Joly, M.; Veron, P., 2004, *A&A*, 417, 515
- Villar Martin, M.; Perna, M.; Humphrey, A.; Castro Rodriguez, N.; Binette, L.; Perez Gonzalez, P. G.; Mateos, S.; Cabrera Lavers, A., 2020, *A&A*, 634, 116
- Yang, Q.; Wu, X.; Fan, X.; et al., 2018, *ApJ*, 862, 109
- Zakamska, N. L.; Hamann, F.; Paris, I.; et al., 2016, *MNRAS*, 459, 3144
- Zhang, X. G., 2014, *MNRAS*, 438, 557
- Zhang, X. G.; Feng, Y. Q.; Chen, H.; Yuan, Q., 2020, *ApJ*, 905, 97
- Zhang, X. G., 2021, *ApJ*, 909, 16, arXiv:2101.02465
- Zhang, X. G., 2021b, *ApJ* accepted, ArXiv:2107.09214
- Zhang, X. G.; Zhang Y. F.; Cheng P. Z.; Wang, B. H.; Lv, Y. L.; Yu, H. C., 2021c, *ApJ* accepted, ArXiv:2109.02189
- Zu, Y.; Kochanek, C. S.; Kozlowski, S.; Udalski, A., 2013, *ApJ*, 765, 106